

# Tailoring Amorphous Boron Nitride for High-Performance 2D Electronics

Cindy Y. Chen,<sup>1</sup> Zheng Sun,<sup>2</sup> Riccardo Torsi,<sup>1</sup> Ke Wang,<sup>3</sup> Jessica Kachian,<sup>4</sup> Bangzhi Liu,<sup>3</sup> Gilbert B. Rayner, Jr,<sup>5</sup> Zhihong Chen,<sup>2</sup> Joerg Appenzeller,<sup>2</sup> Yu-Chuan Lin,<sup>6\*</sup> Joshua A. Robinson<sup>1, 3, 7\*</sup>

1. Department of Materials Science and Engineering, The Pennsylvania State University, University Park, PA 16802, USA
2. School of Electrical and Computer Engineering and Birck Nanotechnology Center, Purdue University West Lafayette, IN 47907, USA
3. Materials Research Institute, The Pennsylvania State University, University Park, PA 16802, USA
4. Intel Corporation, 2200 Mission College Blvd, Santa Clara, CA 95054, USA
5. The Kurt J. Lesker Company, 1925 PA-51, Jefferson Hills, PA 15025, USA
6. Department of Materials Science and Engineering, National Yang Ming Chiao Tung University, Hsinchu City 300, Taiwan
7. Two-Dimensional Crystal Consortium, The Pennsylvania State University, University Park, PA 16802, USA

\*Yu-Chuan Lin (Email: ycl194@nycu.edu.tw)

\*Joshua A. Robinson (Email: jar403@psu.edu)

## Abstract

Two-dimensional (2D) materials have garnered significant attention in recent years due to their atomically thin structure and unique electronic and optoelectronic properties. To harness their full potential for applications in next-generation electronics and photonics, precise control over the dielectric environment surrounding the 2D material is critical. The lack of nucleation sites on 2D surfaces to form thin, uniform dielectric layers often leads to interfacial defects that degrade the device performance, posing a major roadblock in the realization of 2D-based devices. Here, we demonstrate a wafer-scale, low-temperature process (< 250 °C) using atomic layer deposition (ALD) for the synthesis of uniform, conformal amorphous boron nitride (aBN) thin films. ALD deposition temperatures between 125 and 250 °C result in stoichiometric films with high oxidative stability, yielding a dielectric strength of 8.2 MV/cm. Utilizing a seed-free ALD approach, we form uniform aBN dielectric layers on 2D surfaces and fabricate multiple quantum well structures of aBN/MoS<sub>2</sub> and aBN-encapsulated double-gated monolayer (ML) MoS<sub>2</sub> field-effect transistors to evaluate the impact of aBN dielectric environment on MoS<sub>2</sub> optoelectronic and electronic properties. Our work in scalable aBN dielectric integration paves a way towards realizing the theoretical performance of 2D materials for next-generation electronics.

## Introduction

Two-dimensional (2D) materials such as graphene and transition metal dichalcogenides (TMDs) are considered as promising, alternative materials for augmenting conventional Si-based technology due to their atomically thin structure and tunable electronic and optical properties.<sup>1-3</sup> Although promising for the continued scaling of transistors, 2D materials can also present several challenges that prevent the realization of their theoretical performance. First, 2D materials are highly susceptible to ambient instability, as the presence of surface defects can more profoundly impact the 2D material's intrinsic electronic properties compared to that of bulk materials.<sup>4-6</sup> Additionally, the integration of a suitable dielectric environment in 2D material-based transistors is critical for enhancing the carrier transport properties of 2D semiconductors.<sup>7-10</sup> However, the lack of out-of-plane bonding in 2D van der Waals (vdW) surfaces adds considerable difficulty for the integration of gate dielectrics on 2D materials, as the chemical inertness leads to lower growth rates and non-uniform growth of dielectric layers on 2D materials.<sup>11,12</sup> To improve 2D device performance, it is critical to develop an encapsulation process for material passivation and the integration of dielectrics, with specific considerations of back-end-of-line (BEOL) temperature requirement, scalability, reliability, and impact of dielectric environment on 2D electronic properties.

Strategies for dielectric integration include atomic layer deposition (ALD) of 3D amorphous oxides, or transfer of hexagonal boron nitride (hBN) grown via chemical vapor deposition (CVD). ALD of high- $\kappa$  dielectrics such as  $\text{Al}_2\text{O}_3$  and  $\text{HfO}_2$  on TMDs can be carried out on a wafer-scale, at temperature  $< 300$  °C, and with layer-by-layer control. However, water-based precursors are commonly used to synthesize ALD oxides, resulting in the continued possibility of in situ oxidation and degradation of the TMDs.<sup>13</sup> As ALD oxides are 3D in structure, dangling bonds and charged impurities can form at the interface with the 2D semiconductor channel, resulting in the decrease of carrier mobility due to additional charge scattering. In contrast, hBN layers are atomically smooth and can form a clean vdW interface with the 2D semiconducting channel, which can substantially reduce charge carrier scattering due to surface roughness and charged impurities.<sup>14</sup> hBN encapsulation also leads to reduced remote phonon scattering since the high energy surface optical phonon modes of hBN do not couple to the low energy modes in 2D semiconductors.<sup>15</sup>

While hBN is considered a more suitable dielectric material for 2D encapsulation, tradeoffs are present in scalability and thermal requirement, as the CVD of hBN is carried out at high temperatures ( $> 1000$  °C) and on metal templates, and often accompanied by mechanical exfoliation and transfer processes onto the TMD.<sup>16</sup> In comparison, amorphous BN (aBN) can be readily synthesized at low temperature, making it a promising solution for overcoming the stringent processing requirements of hBN. Nevertheless, the scalable synthesis and impact of aBN on 2D semiconductors still requires further investigation.

Here, we present the ALD of ultrathin (2-20 nm) aBN as a scalable, non-water-based, low-temperature process for dielectric integration with 2D semiconductors. We evaluate the impact of ALD processing parameters on the resulting morphology, chemical composition, and structural properties of aBN and demonstrate uniform integration of ultrathin aBN on MoS<sub>2</sub> to enable demonstration of aBN/MoS<sub>2</sub> quantum wells. Finally, we fabricate and characterize ALD aBN-encapsulated double-gated monolayer (ML) MoS<sub>2</sub> transistors with various channel lengths and gate dielectric stacks to study key performance metrics across a large number of devices.

## Results and Discussion

**ALD Synthesis of aBN.** We demonstrate the wafer-scale, uniform, and conformal deposition of BN on planar Si, high-aspect ratio structures, and 2D material surfaces using ALD. BN thin films are deposited using ALD with sequential flows of BCl<sub>3</sub> and NH<sub>3</sub>, which react under the following overall (net) ligand exchange reaction<sup>17-19</sup>:  $\text{BCl}_3 (\text{g}) + \text{NH}_3 (\text{g}) \rightarrow \text{BN} (\text{s}) + 3\text{HCl} (\text{g})$ . A process schematic demonstrating the BN ALD reaction cycle is presented in **Figure 1a**. Unless otherwise specified, BN ALD process and substrate preclean conditions presented in this work are those described under the **Methods** section. Details of the ALD process optimization are described in **Supplementary Figure 1**, where we show that a soak time  $> 2$  s between the precursor pulse and purge steps and between the reactant pulse and purge steps significantly improves adsorbate surface coverage after each half-cycle and yields higher growth rate and wafer-scale thickness uniformity. Due to the surface controlled, self-limiting growth mechanism of ALD,

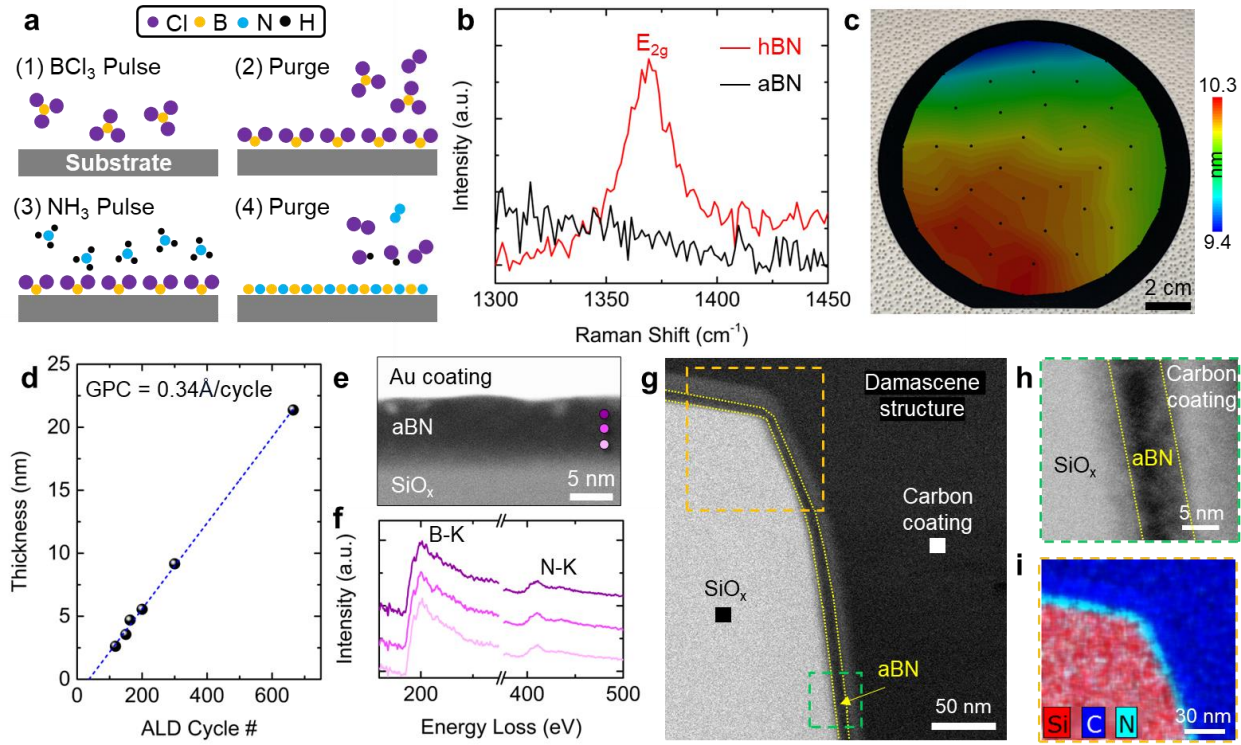


**Figure 1: Wafer-scale atomic layer deposition of amorphous boron nitride.** (a) Schematic illustration of the ALD process for BN thin films. (b) Raman spectra of aBN (black) and hBN (red). The in-plane  $E_{2g}$  vibrational mode of hBN is observed at  $1369\text{ cm}^{-1}$ , which is absent in aBN due to the lack of crystalline order. (c) Camera image and overlaid map of film thickness measured by spectroscopic ellipsometry of as-deposited aBN (300 ALD cycles) on a 150 mm Si wafer. (d) Thickness of aBN deposited at  $250\text{ }^{\circ}\text{C}$  as a function of ALD cycle number. A linear fit (blue) is used to obtain a growth rate of  $0.34\text{ \AA/cycle}$  after the initial nucleation delay. (e) HAADF-STEM cross-sectional image of Au-capped aBN deposited on  $\text{SiO}_x$  at  $250\text{ }^{\circ}\text{C}$  for 300 ALD cycles. (f) EELS characteristics of B-K and N-K from the selected points in (e). (g) HAADF-STEM cross-sectional image of aBN deposited at  $250\text{ }^{\circ}\text{C}$  for 300 ALD cycles on a damascene structure made of  $\text{SiO}_x$ . The aBN is highlighted with yellow dotted lines. (h) Cross-sectional HAADF-STEM image in the green selected area in (g). (i) EDS mapping of Si, C, and N in the orange selected area in (g).

wafer-scale thin films can be deposited with highly controllable thicknesses and low temperature ranges compatible with BEOL process temperatures.<sup>20</sup> The lack of thermal energy in ALD generally inhibits diffusion of precursor molecules,<sup>21</sup> indicating that the BN films will be amorphous or nanocrystalline. For the following structural characterization of ALD-deposited BN, we prepare BN samples deposited at  $250\text{ }^{\circ}\text{C}$  for 300 cycles. The structure of ALD-deposited BN on Si is investigated by Raman spectroscopy using a 532 nm excitation laser and measuring the phonon lines between  $1300 - 1450\text{ cm}^{-1}$ . For structural comparison, we also collect Raman spectra of CVD-grown hBN,<sup>22</sup> which exhibits the characteristic Raman-active in-plane transverse  $E_{2g}$  mode at  $1369\text{ cm}^{-1}$  (**Figure 1b**). The  $E_{2g}$  mode is not observed for the ALD-

deposited BN film, indicating a lack of crystalline order and thus confirms the amorphous nature of the thin film. To assess the scalability of the ALD process, the thickness profile of aBN deposited at 250 °C on a 150 mm Si wafer is mapped with spectroscopic ellipsometry (**Figure 1c**). At 300 ALD cycles, the average thickness is  $9.7 \pm 0.2$  nm across the wafer. We further characterize the ALD growth characteristics of aBN on Si by evaluating the film thickness at different ALD cycle numbers, as shown in **Figure 1d**. After an initial nucleation delay, a linear dependence of the film thickness with increasing ALD cycle is observed, which is consistent with the self-saturating nature of surface reactions during ALD half cycles. The growth rate, defined as the growth per cycle (GPC), is  $0.34 \text{ \AA/cycle}$  based on the slope of the linearly fitted region. This is within the range of GPC values ( $0.32 - 0.42 \text{ \AA/cycle}$ ) reported in previous studies on thermal ALD reactions with  $\text{BCl}_3$  and  $\text{NH}_3$  on Si substrates.<sup>17,23</sup>

The ALD process also enables the conformal coverage of aBN on high-aspect ratio surfaces, a key technological requirement in ultra-scaled applications. Cross-sectional, high-angle annular dark field scanning transmission electron microscopy (HAADF-STEM) is performed to assess the in-plane uniformity of aBN deposited at 250 °C for 300 cycles on  $\text{SiO}_x$ . To provide sufficient contrast for layer distinction, 30 nm Au is thermally evaporated onto the aBN layer. HAADF-STEM image (**Figure 1e**) shows a clear interface between aBN and the  $\text{SiO}_x$  substrate and continuity with no presence of pinholes. The presence of B and N is further confirmed via electron energy loss spectroscopy (EELS) analysis at different points across the film thickness (**Figure 1f**). To assess the effectiveness of the ALD process for conformal aBN deposition, we carry out aBN deposition at 250 °C for 300 cycles on  $\text{SiO}_x$  substrates patterned with  $10 \times 10 \mu\text{m}^2$  trenches 500 nm in depth. The cross-sectional STEM image in **Figure 1g** indicates uniform thickness over the top and sidewall of  $\text{SiO}_x$ , confirming the conformality of aBN. It should be noted that the thin layer of carbon coating on top of aBN is deposited via electron beam evaporation, where the higher density of the carbon layer leads to higher intensity and better contrast for assessment of aBN thickness uniformity on  $\text{SiO}_x$ . As a result, the aBN layer can be clearly observed under the higher-magnification view of the sidewall (**Figure 1h**). Energy-dispersive X-ray spectroscopy (EDS) mapping showing N signals

conformally confined by Si and C signals at the trench edge further validates the uniform deposition of aBN (**Figure 1i**). B signals are not shown due to detection limits of EDS for lighter elements.

**Deposition temperature-dependent properties of aBN.** The growth rate of aBN exhibits dependence on the ALD deposition temperature. In ALD processes, the deposition temperature plays an important role in surface chemistry and reaction kinetics, which in turn dictate the film properties.<sup>24</sup> In this section, we elucidate the impact of deposition temperature, measured from the substrate heater stage, on film properties of aBN deposited from 65 – 250 °C for 300 cycles. The GPC of aBN on a Si wafer increases from 0.31 to 0.59 Å/cycle as the deposition temperature decreases from 250 to 65 °C (**Supplementary Figure 2a**). The higher GPC at low deposition temperatures suggests a deviation from the ALD self-limiting growth behavior, which is likely due to the low-temperature physisorption of multiple monolayers of precursor at the substrate surface.<sup>25,26</sup>

Varying the ALD deposition temperature from 65 – 250 °C does not result in changes in BN crystallinity. We evaluate the film crystallinity by depositing aBN onto amorphous SiO<sub>2</sub> TEM grids for high-resolution transmission electron microscopy (HRTEM) analysis. HRTEM images of aBN deposited from 65 – 250 °C do not exhibit long-range order present in hBN (**Figure 2a-c**). Additionally, diffuse diffraction in selective-area electron diffraction (SAED) patterns further demonstrate the lack of preferred crystallographic orientation (**inset, Figure 2a-c**).

The ALD deposition temperature plays an essential role in oxygen content in aBN films on Si. This is evident using x-ray photoelectron spectroscopy (XPS), where high-resolution spectra in the B 1s region are fit with two components: B-N at 190.5 eV and B-O at 192.4 eV (**Figure 2d**).<sup>27</sup> No B-Cl component, expected at 193.5 eV in the B 1s region, is observed within the detection limit of XPS.<sup>28</sup> The B-O component peak intensity increases as deposition temperature decreases, indicating an increase in the O incorporation into the aBN film. The total O incorporation into the film as quantified from the B-O component increases from 2.1% at 250 °C to 11.4% at 65 °C (**Supplementary Figure 2c**). The O component is not observed in N 1s spectra, where only the N-B component is identified at 398.2 eV, and a low concentration of N-H

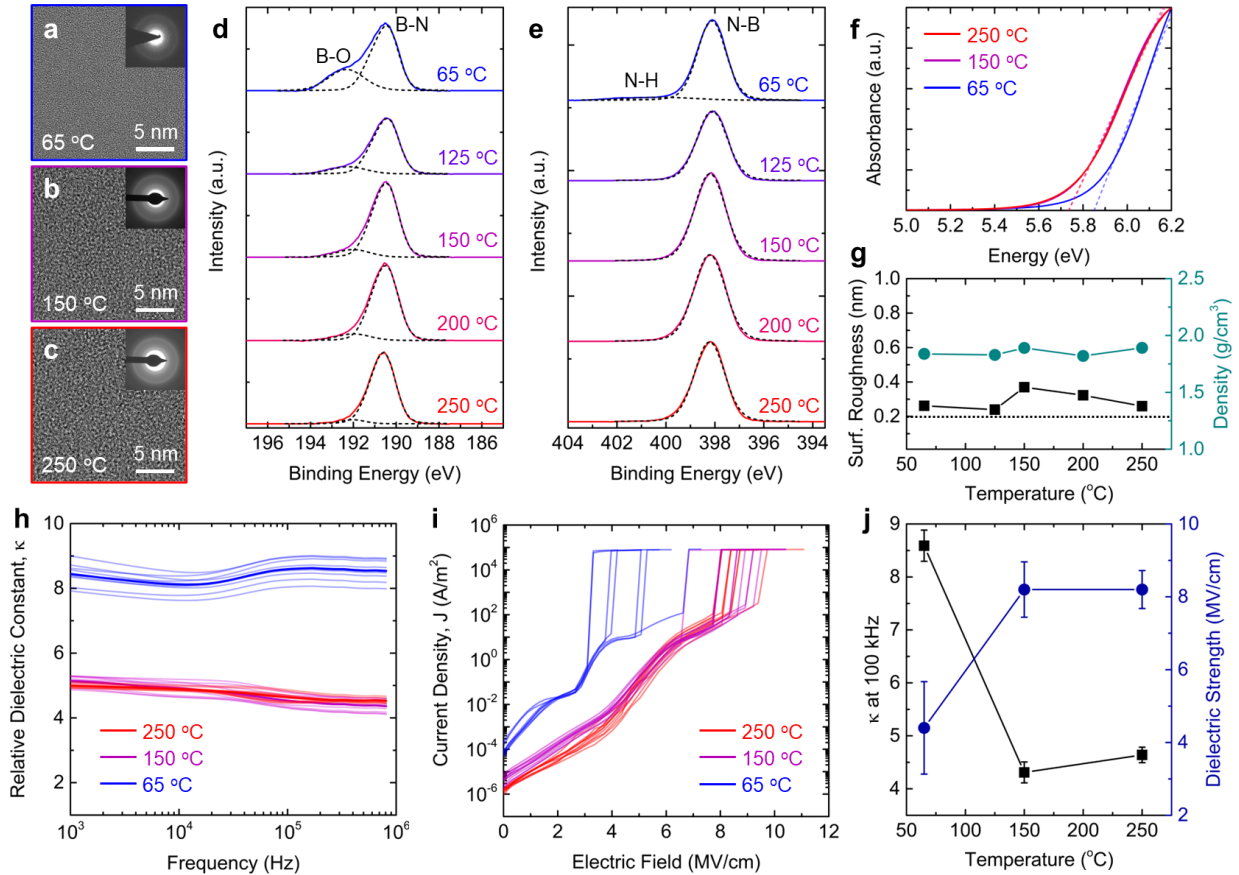


**Figure 2: Deposition temperature-dependent properties of amorphous boron nitride.** Plan-view HRTEM image and the corresponding SAED pattern (inset) of aBN deposited for 300 cycles onto amorphous SiO<sub>2</sub> TEM grids at (a) 65, (b) 150, and (c) 250 °C. (d) B 1s and (e) N 1s core level XP spectra of aBN deposited for 300 cycles on Si from 65 – 250 °C. (f) Tauc plots of aBN with linear fits (dashed lines) for the estimation of aBN optical bandgaps, which are 5.7 eV at 250 and 150 °C, and 5.8 eV at 65 °C. (g) Surface roughness (black) and density (green) of aBN deposited via 300 ALD cycles on Si at 65 – 250 °C. Dotted line shows bare Si substrate roughness for reference. (h) Relative dielectric constant vs. frequency for aBN deposited from 65 – 250 °C for 300 cycles. (i) Current density vs. electric field for dielectric strength of aBN deposited at different temperatures (same deposition conditions as for (h)). (j) Relative dielectric constant at 100 kHz (black) and dielectric strength (blue) of aBN deposited at different temperatures (same deposition conditions as for (h)).

component is identified at 400.2 eV for aBN deposited at 65 °C (**Figure 2e**). The B/N ratio quantified from B and N 1s core level spectra is 0.9 from 125 – 250 °C, and 1.1 at 65 °C (**Supplementary Figure 2b**). The N-deficiency shown in the 65 °C film, combined with the higher detected O at%, suggests that oxidation is favorable when aBN is N-deficient. This is consistent with oxidation of defects in hBN, where N vacancies are decorated with O (O<sub>N</sub>).<sup>29</sup> Compared to other defect systems such as O at B sites (O<sub>B</sub>) or C substitutional defects (C<sub>B</sub> or C<sub>N</sub>), O<sub>N</sub> has the lowest formation energy of 2.20 eV.<sup>30</sup> The N-deficiency shown in the 65 °C film, combined with the higher detected O at%, is also consistent with incomplete ligand exchange at low

deposition temperatures, leading to oxidation of unreacted B-Cl bonds upon air exposure and noting all XPS measurements are ex situ. This model is further supported by the presence of the N-H component of the N 1s peak and the absence of the B-Cl component within the B 1s peak in the XPS of aBN deposited at 65 °C. Based on these results, it is expected that aBN films formed at higher deposition temperatures are stoichiometric and, therefore, more resistant to oxidation. To evaluate this model, which posits that detected aBN oxidation occurs ex situ, we synthesize an aBN stack consisting of an initial deposition at 65 °C, followed by deposition at 200 °C without exposure to ambient. We note that, for aBN deposited at temperatures < 125 °C, the Si concentration approaches the detection limit of the XPS tool (**Supplementary Figure 2c**). This corresponds to an aBN thickness limit of 13 nm, above which the Si substrate is not detectable by XPS. The hybrid aBN film stack is 6.6 nm and yields an oxidation level that is notably reduced compared to that estimated for the hybrid aBN film stack using oxidation levels of the pure 65 °C- (i.e., aBN resulting from deposition at 65 °C only) and pure 200 °C- (i.e., aBN resulting from deposition at 200 °C only) aBN films and accounting for the 65 °C- and 200 °C-aBN ALD thickness contributions to the hybrid aBN film stack (**Supplementary Figure 3**). The estimated (versus measured) O at% in the hybrid aBN film stack is > 2× higher. Note that if oxidation occurs in situ, then the hybrid aBN film stack would yield equal measured and estimated oxidation levels. Consequently, the data supports that observed aBN oxidation occurs ex situ. Further, the data set cannot be used to evaluate the ability of the 200 °C aBN component film of the hybrid aBN film stack to hermetically seal the underlying 65 °C aBN component film. Completing the aforementioned evaluation requires that 200 °C aBN ALD (second ALD step of the in situ hybrid aBN film stack deposition) negligibly transforms the 65 °C aBN component film (deposited in the first ALD step of the in situ hybrid aBN film stack deposition). If this requirement is met, a good hermetic seal would be supported by XPS detection of B-Cl in the underlying 65 °C aBN component film (via a B-Cl binding energy component in the B 1s envelope), and given component film thicknesses, a bad hermetic seal would be supported by equal measured and estimated oxidation levels for the hybrid aBN film stack. That we observe neither the former nor the latter by XPS of the hybrid aBN film stack suggests that 200 °C aBN ALD (second ALD step of the in situ hybrid aBN film stack deposition) significantly



transforms the 65 °C aBN component film (deposited in the first ALD step of the in situ hybrid aBN film stack deposition). This is consistent with the 200 °C aBN ALD step of the in situ hybrid aBN film stack deposition driving increased extent of reaction within the underlying 65 °C aBN component film through elevated temperature allowing unreacted B-Cl and N-H bonds within the 65 °C aBN component film to react with each other and/or with incoming precursors (that can access sites within the 65 °C aBN component film due its thickness at or below minimum continuous thickness or courtesy of diffusion between domains). This is also consistent with similar measured O at% values of 3% (**Supplementary Figure 3**) and 4% (**Supplementary Figure 2c**) for the hybrid aBN film stack and the pure 200 °C aBN film, respectively. Overall, the data in this section support that aBN film deposition solely at higher temperatures or, pending component film thicknesses, in situ hybrid aBN film stack deposition comprised of low- then high-temperature aBN ALD steps yields aBN films or film stacks more resistant to post-growth oxidation, respectively. Therefore, to achieve stoichiometric aBN films or film stacks and maintain high oxidative and hydrolytic stability of aBN, aBN ALD should be performed solely at a deposition temperature within the 125 – 250 °C window or via an in situ hybrid aBN film stack deposition process comprised of relatively thin aBN deposition at 65 °C followed by relatively thick aBN deposition at a temperature within the 125 – 250 °C window.<sup>31</sup> As subsequent sections will show, the latter approach can be used to grow thin aBN films on TMD surfaces without impact to aBN or TMD quality.

aBN films deposited via 300 ALD cycles at 65 – 250 °C on transparent quartz substrates for absorption measurements exhibit a 5.7 – 5.8 eV bandgap (**Figure 2f**). This is comparable to crystalline hBN with bandgaps ranging from 5.6 – 6.0 eV, where the variation is strongly dependent on sample quality and the employed synthesis method.<sup>32–36</sup> Furthermore, we find that the ALD process yields atomically smooth aBN on Si with root-mean-square surface roughness ( $R_q$ ) varying from 0.24 – 0.37 nm across the 65 – 250 °C window (**Figure 2g**, black) with no discernible deposition temperature dependence. The thin film density of aBN on Si, probed using x-ray reflectivity (XRR), does not exhibit any deposition temperature dependence, and varies from 1.8 – 1.9 g/cm<sup>3</sup> from 65 – 250 °C (**Figure 2g**, green). These densities are lower

than the theoretical density of hBN at  $2.1 \text{ g/cm}^3$ , which is likely due to a lower network connectivity of the amorphous phase compared to the layered crystalline phase.

The dielectric response of aBN films varies with ALD deposition temperature for aBN deposited via 300 cycles of ALD on  $\text{p}^{++}\text{-Si}$  at 65, 150, and 250 °C. The capacitance measurements of Pt/aBN/ $\text{p}^{++}\text{-Si}$  metal-insulator-semiconductor (MIS) stacks from  $10^3 - 10^6$  Hz demonstrate the extracted relative dielectric constant,  $\kappa$ , decreases by ~10% for aBN deposited at 250 and 150 °C, but exhibits a  $2\times$  increase at 65 °C (**Figure 2h**), suggesting a different polarizability mechanism at low deposition temperatures. The  $\kappa$  value at 100 kHz is 4.3, 4.6, and 8.6 for 250, 150, and 65 °C, respectively. Under an applied bias, we see the current density of aBN films increases steadily until dielectric breakdown to current saturation (**Figure 2i**). The calculated dielectric strength is 4.4 MV/cm at 65 °C, and 8.2 MV/cm for 150 °C and 250 °C. The relative dielectric constant  $\kappa$  at 100 kHz and dielectric strength at different aBN deposition temperatures are summarized in **Figure 2j**. Only the 65 °C aBN film exhibits anomalous dielectric performance, with both a low dielectric breakdown strength and high  $\kappa$  value. To date, aBN is reported to exhibit dielectric constants of 1.8 – 5.5.<sup>37-40</sup> The observed changes in dielectric properties may be due to several factors, including material crystallinity, density, and composition. Because ALD-aBN density and physical structure remain constant across the investigated temperature window, these may be ruled out as the dominating factor for dielectric response changes. However, the aBN does exhibit increased O incorporation with decreasing deposition temperature. The O level can have a direct impact on the dielectric properties of aBN.  $\text{O}_\text{N}$  defects, for instance, introduce defect levels near the conduction band, thereby enhancing the material's metallic characteristics.<sup>30,41</sup> This, in turn, can create conductive pathways in the band structure of aBN thin films, leading to the observed, and highly variable, low-field breakdown. ALD-aBN deposited at temperatures  $> 150$  °C features excellent structural and dielectric strength compared to other reported forms of BN thin films.<sup>22,39</sup>

**Fabrication and characterization of aBN/MoS<sub>2</sub> quantum wells.** A modified, two-step, ALD process enables seed-free formation of ultrathin, continuous aBN dielectric layers on 2D material surfaces. This enables fabrication of aBN-based devices, including aBN/MoS<sub>2</sub> quantum well stacks (**Figure 3a**).<sup>42</sup> Utilizing the 65 °C aBN as the nucleating interfacial layer, we can subsequently deposit uniform, stoichiometric aBN at 250 °C on MoS<sub>2</sub>. The optimal 65 °C ALD cycle number, based on AFM analysis of surface uniformity and film coalescence, is 40 (**Figure 3b-c**, and **Supplementary Figure 4**). XPS analysis of aBN/MoS<sub>2</sub> in the Mo 3d and S 2p regions indicate a decrease in Mo and S intensities after aBN encapsulation, which is expected due to the attenuation of photoelectrons from the dielectric layer (**Supplementary Figure 5**). Normalized XP spectra reveal a binding energy shift of  $-0.34$  eV in Mo 3d<sub>5/2</sub>

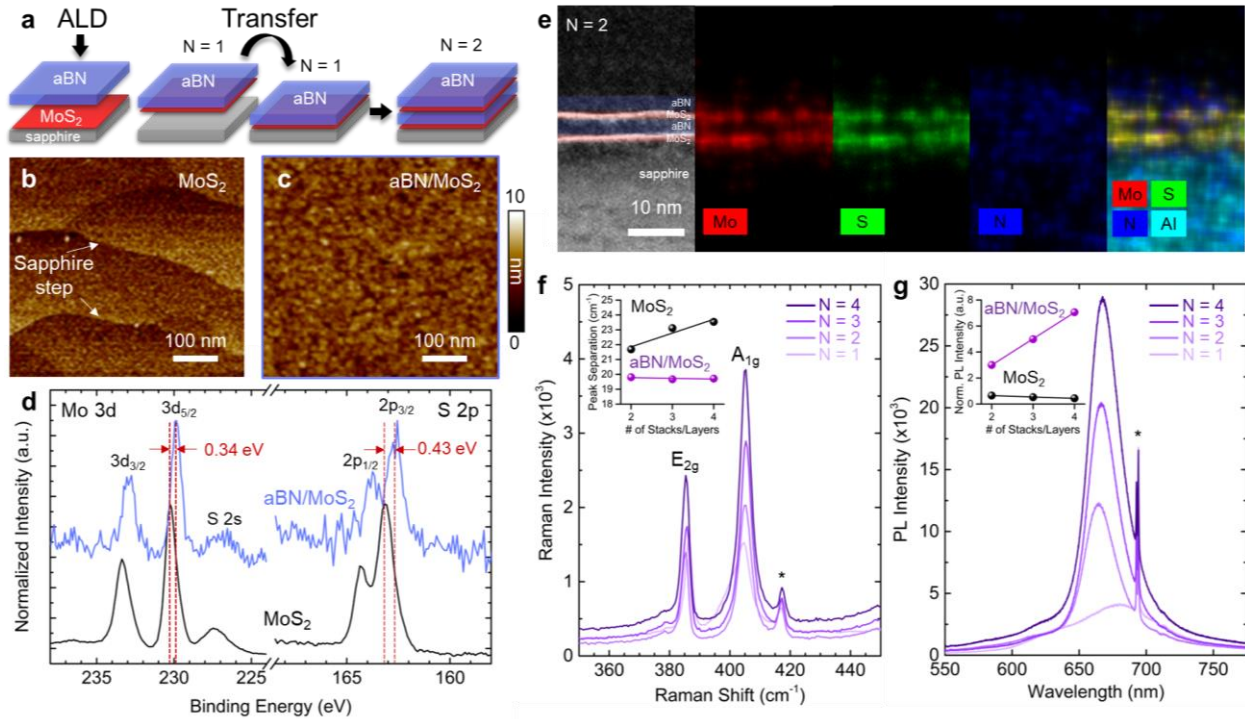


**Figure 3: Integration of aBN with MoS<sub>2</sub> for evaluation of optoelectronic properties.** (a) Schematic diagram of the synthesis of aBN/MoS<sub>2</sub> superlattices. AFM image of (b) as-grown monolayer MoS<sub>2</sub> and (c) aBN deposited on MoS<sub>2</sub>. (d) Mo 3d and S 2p XPS spectra of as-grown MoS<sub>2</sub> (black) and after aBN deposition (blue) with the same process conditions as (c). (e) Cross-sectional HAADF-STEM image and corresponding EDS mapping of N = 2 aBN/MoS<sub>2</sub> superlattices on  $\alpha$ -Al<sub>2</sub>O<sub>3</sub>. (f) Raman spectra in the range of MoS<sub>2</sub> E<sub>2g</sub> and A<sub>1g</sub> vibrational peaks for N = 1 – 4 stacks of aBN/MoS<sub>2</sub>. (g) PL spectra of N = 1 – 4 stacks of aBN/MoS<sub>2</sub> showing increasing intensity as N increases. In (f) and (g), \* denotes the signal from the sapphire substrate, and the insets present a comparative analysis between multilayer MoS<sub>2</sub> and aBN/MoS<sub>2</sub> stacks. The PL intensity for MoS<sub>2</sub> in the inset of (g) is adapted from Ref. <sup>46</sup>.

and  $-0.43$  eV in S  $2p_{3/2}$  after aBN encapsulation (**Figure 3d**). Additionally, no other defect peaks are detected, indicating the compatibility of the ALD-aBN process in preserving the as-grown quality of monolayer MoS<sub>2</sub>. The quantum well structures, using a stack of barrier/semiconductor/barrier as the building block, exhibit enhanced photoluminescence (PL) emission with each additional stack, indicating we are able to tune the light-matter coupling of 2D semiconducting TMDs.<sup>43,44</sup> We first confirm the formation of  $N = 2$  aBN/MoS<sub>2</sub> superlattice after the first dry transfer step using cross-sectional HAADF-STEM and the corresponding EDS mapping of Mo, S, N, and Al signals (**Figure 3e**). The estimated thicknesses from STEM images are 0.7 and 2.5 nm for the MoS<sub>2</sub> and aBN layers, respectively, validating the separation of monolayer MoS<sub>2</sub> with ultrathin aBN dielectric layers. The structural integrity of the monolayer MoS<sub>2</sub> after aBN encapsulation can also be confirmed by the observed  $E_{2g}$  and  $A_{1g}$  Raman modes of MoS<sub>2</sub> at  $386.5$   $\text{cm}^{-1}$  and  $404.5$   $\text{cm}^{-1}$ , respectively, for the  $N = 1$  stack. As  $N$  increases, the Raman intensity increases and the FWHM narrows for  $N > 1$  stacks due to strain release of the monolayer MoS<sub>2</sub> from the transfer process (**Figure 3f** and **Supplementary Figure 6**). The preservation of monolayer MoS<sub>2</sub> characteristics is also verified by the peak separation between  $E_{2g}$  and  $A_{1g}$ , which remains constant at  $19.7$   $\text{cm}^{-1}$ , a stark difference from multilayer MoS<sub>2</sub> where the peak separation increases linearly as layer number increases (**Figure 3f**, inset). The increasing trend in peak separation is calculated from the Raman peaks of our MOCVD-grown multilayer MoS<sub>2</sub> (**Supplementary Figure 7**) and is similarly observed in exfoliated MoS<sub>2</sub> flakes.<sup>45</sup> As a result of the monolayer MoS<sub>2</sub> confinement, increasing the repeating unit  $N$  leads to a linear increase in the PL intensity (**Figure 3g**). This points to an improvement in the probability of carrier recombination via dielectric integration with aBN, contrary to multilayer MoS<sub>2</sub> where PL intensity decreases with increasing layer number (**Figure 3g**, inset) due to direct-to-indirect bandgap transition.<sup>46</sup> Once again, the  $N = 1$  PL peak displays peak broadening with an excitonic wavelength of  $681.0$  nm, or  $1.82$  eV, due to substrate strain effects of as-grown monolayer MoS<sub>2</sub>. Following the dry transfer and stacking, the PL spectra all remain at  $1.86$  eV from  $N = 2 - 4$ , consistent with other reports of monolayer MoS<sub>2</sub> at  $1.85$  eV, with no change in the electronic structure of MoS<sub>2</sub> from direct-to-indirect bandgap due to quantum

well formation.<sup>47</sup> This demonstration shows that ALD aBN with controllable thickness can be applied to scalable TMD superlattice fabrication in place of CVD-grown hBN, Al<sub>2</sub>O<sub>3</sub> dielectric, or WO<sub>x</sub>.<sup>43,44</sup>

**Transport properties of aBN-encapsulated MoS<sub>2</sub> FETs.** Near ideal transport characteristics are observed in ALD aBN-encapsulated monolayer MoS<sub>2</sub> field effect transistors (FETs). We fabricate sets of double-gated ML MoS<sub>2</sub> FETs with aBN/HfO<sub>2</sub> stacks as gate dielectrics. Schematic illustrations of FETs at different process stages are shown in **Figure 4a**: i) On the left: back-gated ML MoS<sub>2</sub> FET with HfO<sub>2</sub> gate dielectric; On the right: back-gated ML MoS<sub>2</sub> FET with an aBN/HfO<sub>2</sub> stack as gate dielectric; ii) an aBN layer deposited on top of the back-gated ML MoS<sub>2</sub> FET with an aBN/HfO<sub>2</sub> stack as gate dielectric; and iii) a double-gated ML MoS<sub>2</sub> FET formed by depositing HfO<sub>2</sub> then top gate metal onto the stack shown in ii). Because of the relatively small bandgap of aBN and potential for gate leakage, a stack of aBN/HfO<sub>2</sub> (3.6 nm/5.5 nm) is used to enable high carrier densities in the MoS<sub>2</sub> channel. The transfer curves of FETs with different channel lengths are shown in **Figure 4b**. At V<sub>ds</sub> = 1.0 V, the threshold voltage (V<sub>th</sub>) shows little variation from device to device. The on-current level exhibits a clear dependence on channel length as shown in the linear plot corresponding to the right y-axis. Drain induced barrier lowering (DIBL) of only 55 mV/V at 1 nA is observed for a L<sub>ch</sub> ~ 800 nm ML MoS<sub>2</sub> FET, as shown in **Figure 4c**, and the device shows a good on/off current ratio of up to 10<sup>9</sup>. **Figure 4d** presents the full range subthreshold slope (SS) versus I<sub>ds</sub> for all devices characterized, again showing small device-to-device variations. The minimum SS for all channel lengths is close to 60 mV/dec at 10<sup>-5</sup> μA/μm, which indicates good electrostatic control from the back gate and limited amount of trap charges from the bottom dielectric layer, not exceeding 10<sup>12</sup> cm<sup>-2</sup>. By fabricating double-gated transistors, we also proved that aBN can be used as a top intermediate layer for subsequent HfO<sub>2</sub> deposition. Previous studies using a metal oxide seeding layer on MoS<sub>2</sub> showed significant off-state degradation due to trapped charges at the MoS<sub>2</sub> interfaces induced by oxygen defects in the metal oxide seeding layer.<sup>48,49</sup> Benefiting from the ALD growth of aBN, defect states are well controlled. **Figure 4e** shows the performance of an exemplary dual-gate controlled ML MoS<sub>2</sub> FET for the same device before and after top gate formation. The double gate structure enables an about two times

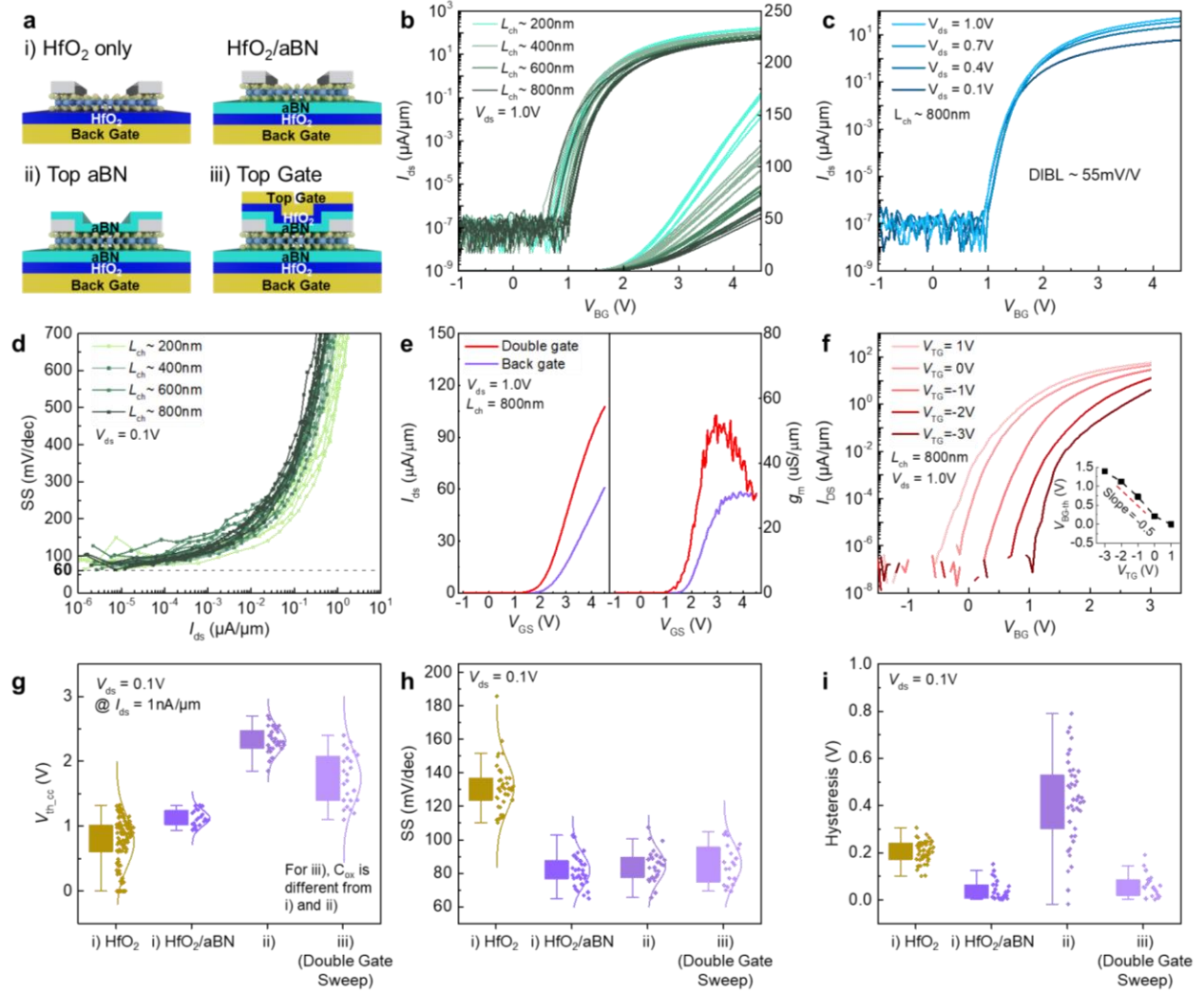


**Figure 4: Amorphous Boron Nitride encapsulated monolayer MoS<sub>2</sub> FETs.** (a) Schematic representation of i) back-gated ML MoS<sub>2</sub> FET with HfO<sub>2</sub> (left) and an aBN/HfO<sub>2</sub> stack (right) as gate dielectrics, ii) the aBN layer on top of MoS<sub>2</sub> FETs shown on the right in i), and iii) the double-gated ML (monolayer) MoS<sub>2</sub> FET. (b) Transfer characteristics of ML MoS<sub>2</sub> FETs with different channel lengths on aBN/HfO<sub>2</sub> substrate (back gate only as illustrated in (a) i) on the right). (c) Transfer curves of a ML MoS<sub>2</sub> FET with  $L_{ch} \sim 800\text{nm}$  at different  $V_{ds}$  (see (a) i) on the right). (d) Full range SS versus  $I_{ds}$  for different channel length FETs (see (a) i) on the right). (e) Transfer curves and transconductance plots of a ML MoS<sub>2</sub> FET (back gate versus double gate). (f) Transfer characteristics of a top-gate modulated ML MoS<sub>2</sub> FET. The inset shows the threshold voltage  $V_{BG-th}$  versus  $V_{TG}$ . (g) Distribution of  $V_{th-cc}$  at constant current for four types of ML MoS<sub>2</sub> FETs shown in (a); From left to right: i) ML MoS<sub>2</sub>/HfO<sub>2</sub>/back gate, i) ML MoS<sub>2</sub>/aBN/HfO<sub>2</sub>/back gate, ii) aBN/ML MoS<sub>2</sub>/aBN/HfO<sub>2</sub>/back gate, and iii) top gate/HfO<sub>2</sub>/aBN/ML MoS<sub>2</sub>/aBN/HfO<sub>2</sub>/back gate. (h) SS-distribution of ML MoS<sub>2</sub> FETs. (i) Hysteresis-distribution of ML MoS<sub>2</sub> FETs.

higher current level compared with the “only back gate” structure as expected for the increased oxide capacitance. Using the same sweep range of  $V_{BG}$ ,  $V_{th-cc}$  can be continuously changed by the top gate. The extracted  $V_{BG-th}$  versus  $V_{TG}$  dependence at 1 nA/ $\mu\text{m}$  is plotted in the inset of **Figure 4f** showing a slope of

about -0.5. Theoretically, the slope should be equal to the capacitance ratio between the top and the bottom dielectric. Since both the top dielectric and the bottom dielectric have the same dielectric stack with 3.6 nm aBN and 5.5 nm HfO<sub>2</sub>, the expected slope of  $V_{BG-th}/V_{TG}$  is -1. The smaller experimental slope implies a smaller total capacitance of the top gate dielectric stack, which is likely related to interface traps at the top interface/s, since the subthreshold slope as a function of top gate voltage alone is found to be significantly larger than the one as a function of back gate voltage alone, as shown in **Supplementary Figure 8**. More research is required to fully understand this phenomenon. To further characterize the impact of aBN as an interfacial layer, it is important to carefully study its impact on the  $V_{th}$  and SS, since previous reports have shown deteriorated SS and negatively shifted  $V_{th}$  for both AlO<sub>x</sub> and TaO<sub>x</sub> seeding layers.<sup>50</sup> From **Figure 4g**, we observe a slightly positive shift of  $V_{th\_cc}$  after aBN deposition, and after the top gate formation, the  $V_{th\_cc}$  exhibits a larger threshold voltage variation compared with only back gated devices, which is likely related to the higher interface trap density at the top gate as discussed above. Compared with the HfO<sub>2</sub> only substrates, the HfO<sub>2</sub>/aBN dielectric stack has a much narrower distribution of threshold voltages, again attesting to the benefits of employing aBN as an interfacial layer between HfO<sub>2</sub> and the TMD. For the SS, as shown in **Figure 4h**, there is no deterioration after aBN deposition and after top gate formation. (Note that in case of iii), both gates are tied together, which compensates for the above discussed deteriorated SS when the top gate alone is used). In fact, the HfO<sub>2</sub>/aBN dielectric stack allows for better SS, if compared with the HfO<sub>2</sub> only substrates. In **Figure 4i**, we also compare the hysteresis distribution of the HfO<sub>2</sub> only and HfO<sub>2</sub>/aBN stack, including after aBN deposition and after top gate formation. We find that devices fabricated on the HfO<sub>2</sub>/aBN stack show a very small hysteresis and narrow distribution among devices. However, after the deposition of the top aBN interfacial layer, the devices exhibit larger hysteresis due to deposition-induced charges. This is not inconsistent with the findings in **Figure 4h**, since in this figure, the SS values for ii) were extracted only from the “positive-to-negative” gate voltage sweep. The much-improved gate control in case iii) allows to recover the small hysteretic behavior as expected.

## Conclusion

In conclusion, we have developed a wafer-scale, low-temperature ALD process for atomically smooth and conformal aBN dielectric for integration with 2D material-based electronics. We established the deposition temperature as a critical factor in controlling the aBN chemical composition, which in turn dictates the dielectric response of aBN. Quantum confinement of MoS<sub>2</sub> with aBN leads to enhanced Raman and PL intensities that increase linearly with the stacking number in scalable MoS<sub>2</sub>/aBN quantum well structures. Additionally, we have demonstrated that ALD aBN serves as an interfacial layer for monolayer MoS<sub>2</sub> transistors, delivering excellent off-state performance, including a close-to-ideal subthreshold slope and minimal threshold voltage variations. We successfully demonstrated a double-gated monolayer MoS<sub>2</sub> transistor encapsulated by ALD aBN, exhibiting excellent performance specs. Overall, our work paves a route towards scalable integration of dielectrics for the realization of advanced 2D-based electronics.



## Methods

### Substrate Preparation

Si substrates (University Wafer, Inc.) are cleaned by sonication in acetone, isopropyl alcohol, and DI water for 10 min each. SiO<sub>2</sub> (10 μm)/Si substrates (University Wafer, Inc.) for trench patterning are cleaned with PRS-3000 for 10 min at 60 °C, followed by room temperature rinse in isopropyl alcohol and DI water for 2 min each. After pre-baking at 180 °C for 5 min, MaN-2405 resist is spin coated on the sample at 3000 rpm for 45 s and soft-baked at 90 °C for 2 min. Pattern is exposed using electron beam lithography (Raith EBPG-5200) with a dose of 700 uC/cm<sup>2</sup>, then developed in CD-26 for 2 min and rinsed with DI water. For enhanced etch selectivity of SiO<sub>2</sub>, 150 nm of Cr hard mask is deposited via evaporation (Temescal F-2000), followed by lift-off using PRS3000. SiO<sub>2</sub> is etched with CF<sub>4</sub> (Plasma-Therm Versalock700), resulting in a trench depth of 500 nm. Cr is removed with Cr etchant 1020 at room temperature for 15 min, followed by DI water rinse. Prior to aBN deposition, patterned SiO<sub>2</sub>/Si substrates are cleaned by sonication in acetone, isopropyl alcohol, and DI water for 10 min each.

### ALD aBN Synthesis

The ALD of BN is performed in a Kurt J. Lesker ALD150LX perpendicular-flow reactor. An Ebara ESR20N dry pump (nominal pumping speed: 46-70 cfm, base pressure: 15 mTorr) is used to pump down the chamber. All upstream ports are sealed by either metal seals or differentially pumped O-ring seals to minimize air permeation as described in Ref.<sup>51</sup>. 99.999% pure Ar is used as a carrier gas, which is further purified by passing through an inert gas purifier (Entegris Gatekeeper GPU70 316LSS). The process pressure is maintained at ~1.0 Torr. BCl<sub>3</sub> (Praxair, 99.999%) and NH<sub>3</sub> (Linde, 99.995%) are used for B and N sources, respectively. NH<sub>3</sub> is purified by passing through a MicroTorr MC1-703FV purifier. Two stage step-down delivery systems are built for both BCl<sub>3</sub> and NH<sub>3</sub> to reduce the dosing pressure to about 50 mTorr above the process pressure. Static dosing is performed for both BCl<sub>3</sub> and NH<sub>3</sub> precursors, including pulse and soak steps with no active pumping. The ALD cycle consists of the following six steps: (1) 1 s BCl<sub>3</sub>

pulse, (2) 2 s soak, (3) 10 s purge, (4) 2 s NH<sub>3</sub> pulse, (5) 2 s soak, (6) 60 s purge. The Ar carrier gas flows for pulse and purge steps are 15 and 25 sccm, respectively.

### **MOCVD MoS<sub>2</sub> Growth**

Monolayer MoS<sub>2</sub> material for aBN/MoS<sub>2</sub> quantum well structures is grown via MOCVD. A custom-built MOCVD system is utilized to grow monolayer MoS<sub>2</sub> films on 1 cm<sup>2</sup> c-plane sapphire substrates (Cryscore Optoelectronic Ltd, 99.996%). Mo(CO)<sub>6</sub> (99.99%, Sigma-Aldrich) serves as the Mo precursor and H<sub>2</sub>S (99.5%, Sigma-Aldrich) provides sulfur during synthesis. Details of the growth process for achieving uniform monolayer MoS<sub>2</sub> films have been previously described in our publication.<sup>52</sup>

### **Layer Transfer and Quantum Well Fabrication**

aBN deposition on MoS<sub>2</sub> consists of 40 cycles of 65 °C aBN ALD followed by 225 cycles of 250 °C aBN ALD. To transfer the aBN/MoS<sub>2</sub> films and fabricate quantum well structures, the samples are first coated with a layer of PMMA (Micro Chem. 950K A6) using a two-step spin casting process (step 1: 500 rpm for 15 s; step 2: 4500 rpm for 45 s). The PMMA/aBN/MoS<sub>2</sub> stack is then baked at 90 °C for 10 min. Next, thermal release tape (TRT) (Semiconductor Corp., release temperature 120 °C) is carefully placed on the top PMMA layer. The stack is then transferred to a DI water sonication bath for 15 min, facilitating the separation of the growth substrate. Subsequently, the TRT/PMMA/aBN/MoS<sub>2</sub> stack is thoroughly dried with N<sub>2</sub> to eliminate any water present at the interface prior to careful transfer onto the target substrate. After ensuring proper adhesion to the target substrate, the TRT is removed by heating it above its release temperature on a hot plate at 130 °C. The PMMA layer is removed by dissolving in acetone for 8 h. The sample is then rinsed in IPA and dried on a hot plate at 80 °C. The entire transfer process is repeated N times to realize (N + 1) aBN/MoS<sub>2</sub> quantum well structures.

### **Spectroscopic Ellipsometry**

Film thickness and refractive index are evaluated using spectroscopic ellipsometry (J. A. Woollam M-2000) carried out from 192 to 1000 nm. The Cauchy model is used to extract the thickness and refractive index of the BN layer.

### **X-ray Photoelectron Spectroscopy**

Chemical composition is measured by x-ray photoelectron spectroscopy (Physical Electronics VersaProbe II) with Al  $K_{\alpha}$  monochromatic excitation source and a spherical sector analyzer. All spectra are charge corrected to C 1s spectrum at 284.8 eV.

### **Raman Spectroscopy and Photoluminescence**

Raman and PL spectra are obtained using the Horiba Scientific LabRam HR Evolution VIS-NIR instrument with a laser wavelength of 532 nm at 3.4 mW for 10 s and 0.34 mW for 5 s, respectively.

### **Transmission Electron Microscopy**

The microstructures of the cross-sectional samples are observed by FEI Titan3 G2 double aberration-corrected microscope at 300 kV. All scanning transmission electron microscope (STEM) images are collected by using a high-angle annular dark field (HAADF) detector which has a collection angle of 52-253 mrad. EDS elemental maps of the sample are collected by using a SuperX EDS system under STEM mode. The electron energy loss spectroscopy (EELS) is performed under STEM mode by using a GIF Quantum 963 system. Thin cross-sectional TEM specimens are prepared by using focused ion beam (FIB, FEI Helios 660) lift-out technique. A thick protective amorphous carbon layer is deposited over the region of interest then Ga<sup>+</sup> ions (30 kV then stepped down to 1 kV to avoid ion beam damage to the sample surface) are used in the FIB to make the samples electron transparent. The plane-view TEM (high resolution TEM (HRTEM) imaging, and the corresponding selected area electron diffraction (SAED) patterns) is performed on a FEI Talos F200x TEM at 200 kV.

### **Absorbance Measurement**

The absorbance spectrum is measured using an Agilent/Cary 7000 spectrophotometer for aBN directly deposited on double-side polished transparent quartz substrates (University Wafer, Inc.).

### **X-ray Reflectivity**

X-ray reflectivity (XRR) spectra of aBN deposited on Si are collected using Malvern Panalytical X'Pert3 MRD with Cu  $K_{\alpha}$  source at 40 mA and 45 kV. Spectra are fitted using the X'Pert Reflectivity software.

### **Atomic Force Microscopy**

Atomic force microscopy (AFM) is conducted using Bruker Dimension Icon instrument with a RTESPA-150 tip in peak-force tapping mode. AFM scans are collected with a peak force setpoint of 1.00 nN and a scan rate of 1.00 Hz.

### **Dielectric Constant and Breakdown Voltage Measurements**

Dielectric characterization of aBN is carried out on Pt/aBN/p-Si device structures. p-Si substrate is treated with buffered oxide etch (BOE 6:1) for 5 min to remove surface native oxide, then rinsed with DI water and dried with  $N_2$  gas. The p-Si substrate is immediately transferred to the ALD chamber for direct deposition of aBN. A shadow mask with 200  $\mu\text{m}$  diameter holes is used to sputter 200 nm thick Pt electrodes onto aBN/p-Si. C-f measurements of Pt/aBN/p-Si are measured from 1 kHz to 1 MHz at 30 mV using Agilent HP4980 Precision LCR Meter. I-V characteristics are measured using the HP4140B pA meter.

### **Double-Gated Monolayer MoS<sub>2</sub> FET Fabrication and Analysis**

Monolayer MoS<sub>2</sub> material for FET fabrication is purchased from 2D semiconductors. ML MoS<sub>2</sub> single crystals are wet transferred on to the local bottom gate substrates. The local bottom gate substrates consist of a stack of Cr/Au (2/13 nm) as gate metal and 5.5 nm HfO<sub>2</sub> and 3.6 nm aBN as dielectric layer grown by

ALD. aBN deposition consists of 150 cycles of 250 °C aBN ALD. After the wet transfer process, the sample is annealed at a pressure of  $\sim 5 \times 10^{-8}$  Torr at 200 °C for 2 h. Optical microscopy is used to identify flakes located on local bottom gates and the sample is spin coated with photoresist PMMA and baked at 180 °C for 5 mins. Next, source/drain contacts are patterned by a JEOL JBX-8100FS E-Beam Writer system and developed in an IPA/DI solution followed by e-beam evaporation of 70 nm Ni as contact metal. Next, the sample undergoes a lift-off process. To fabricate a top gate hybrid stack of aBN/HfO<sub>2</sub>, 3.6 nm aBN and 5.5 nm HfO<sub>2</sub> are deposited by ALD. The top aBN deposition consists of 40 cycles of 65 °C aBN ALD followed by 90 cycles of 200 °C aBN ALD. Finally, the top gate metal is defined by e-beam lithography (EBL), and e-beam evaporation of 50 nm Ni, followed by another lift-off process in acetone. Details of the FET fabrication process flow have been described previously.<sup>48</sup> A Lake Shore CPX-VF probe station and Agilent 4155C Semiconductor Parameter Analyzer are used to perform the electrical characterization at room temperature in high vacuum ( $\approx 10^{-6}$  Torr). Standard DC sweeps are used in the electrical measurements for all devices. All devices are measured as fabricated.

## References

1. Akinwande, D. *et al.* Graphene and two-dimensional materials for silicon technology. *Nature* **573**, 507–518 (2019).
2. An, J. *et al.* Perspectives of 2D Materials for Optoelectronic Integration. *Adv Funct Mater* **32**, (2022).
3. Lemme, M. C., Akinwande, D., Huyghebaert, C. & Stampfer, C. 2D materials for future heterogeneous electronics. *Nat Commun* **13**, (2022).
4. Longo, R. C. *et al.* Intrinsic air stability mechanisms of two-dimensional transition metal dichalcogenide surfaces: Basal versus edge oxidation. *2d Mater* **4**, (2017).
5. Li, Q., Zhou, Q., Shi, L., Chen, Q. & Wang, J. Recent advances in oxidation and degradation mechanisms of ultrathin 2D materials under ambient conditions and their passivation strategies. *J Mater Chem A Mater* **7**, 4291–4312 (2019).
6. Ahn, J. H., Parkin, W. M., Naylor, C. H., Johnson, A. T. C. & Drndić, M. Ambient effects on electrical characteristics of CVD-grown monolayer MoS<sub>2</sub> field-effect transistors. *Sci Rep* **7**, (2017).
7. Li, W. *et al.* Uniform and ultrathin high- $\kappa$  gate dielectrics for two-dimensional electronic devices. *Nat Electron* **2**, 563–571 (2019).
8. Knobloch, T. *et al.* The performance limits of hexagonal boron nitride as an insulator for scaled CMOS devices based on two-dimensional materials. *Nat Electron* **4**, 98–108 (2021).
9. Illarionov, Y. Y. *et al.* Insulators for 2D nanoelectronics: the gap to bridge. *Nat Commun* **11**, (2020).
10. Sun, Z., Chen, C., Robinson, J. A., Chen, Z. & Appenzeller, J. A mobility study of monolayer MoS<sub>2</sub> on low- $\kappa$ /high- $\kappa$  dielectrics. in *2023 Device Research Conference (DRC)* 1–2 (IEEE, 2023). doi:10.1109/DRC58590.2023.10258241.
11. Yang, S. *et al.* Gate Dielectrics Integration for Two-Dimensional Electronics: Challenges, Advances and Outlook. *Advanced Materials* **35**, 2207901 (2023).
12. McDonnell, S. *et al.* HfO<sub>2</sub> on MoS<sub>2</sub> by atomic layer deposition: Adsorption mechanisms and thickness scalability. *ACS Nano* **7**, 10354–10361 (2013).

13. Walter, T. N., Kwok, F., Simchi, H., Aldosari, H. M. & Mohny, S. E. Oxidation and oxidative vapor-phase etching of few-layer MoS<sub>2</sub>. *Journal of Vacuum Science & Technology B* **35**, (2017).
14. Bresnehan, M. S. *et al.* Integration of hexagonal boron nitride with quasi-freestanding epitaxial graphene: Toward wafer-scale, high-performance devices. *ACS Nano* **6**, 5234–5241 (2012).
15. Ma, N. & Jena, D. Charge scattering and mobility in atomically thin semiconductors. *Phys Rev X* **4**, (2014).
16. Kim, K. K., Lee, H. S. & Lee, Y. H. Synthesis of hexagonal boron nitride heterostructures for 2D van der Waals electronics. *Chem Soc Rev* **47**, 6342–6369 (2018).
17. Uene, N. *et al.* Growth mechanism study of boron nitride atomic layer deposition by experiment and density functional theory. *Comput Mater Sci* **217**, (2023).
18. Ferguson, J. D., Weimer, A. W. & George, S. M. Atomic layer deposition of boron nitride using sequential exposures of BCl<sub>3</sub> and NH<sub>3</sub>. *Thin Solid Films* **413**, 16–25 (2002).
19. Bull, S. K. *et al.* Atomic layer deposited boron nitride nanoscale films act as high temperature hydrogen barriers. *Appl Surf Sci* **565**, (2021).
20. George, S. M. Atomic layer deposition: An overview. *Chem Rev* **110**, 111–131 (2010).
21. Miikkulainen, V., Leskelä, M., Ritala, M. & Puurunen, R. L. Crystallinity of inorganic films grown by atomic layer deposition: Overview and general trends. *J Appl Phys* **113**, (2013).
22. Bansal, A. *et al.* Substrate modification during chemical vapor deposition of hBN on sapphire. *ACS Appl Mater Interfaces* **13**, 54516–54526 (2021).
23. Lee, J. *et al.* Atomic Layer Deposition of Layered Boron Nitride for Large-Area 2D Electronics. *ACS Appl Mater Interfaces* **12**, 36688–36694 (2020).
24. Miikkulainen, V., Leskelä, M., Ritala, M. & Puurunen, R. L. Crystallinity of inorganic films grown by atomic layer deposition: Overview and general trends. *J Appl Phys* **113**, (2013).
25. Johnson, R. W., Hultqvist, A. & Bent, S. F. A brief review of atomic layer deposition: From fundamentals to applications. *Materials Today* **17**, 236–246 (2014).

26. Nam, T., Seo, S. & Kim, H. Atomic layer deposition of a uniform thin film on two-dimensional transition metal dichalcogenides. *Journal of Vacuum Science & Technology A: Vacuum, Surfaces, and Films* **38**, (2020).
27. Shankar, R., Marchesini, S. & Petit, C. Enhanced Hydrolytic Stability of Porous Boron Nitride via the Control of Crystallinity, Porosity, and Chemical Composition. *Journal of Physical Chemistry C* **123**, 4282–4290 (2019).
28. Silva-Quinones, D., He, C., Butera, R. E., Wang, G. T. & Teplyakov, A. V. Reaction of BCl<sub>3</sub> with H- and Cl-terminated Si(100) as a pathway for selective, monolayer doping through wet chemistry. *Appl Surf Sci* **533**, (2020).
29. Weston, L., Wickramaratne, D., Mackoite, M., Alkauskas, A. & Van De Walle, C. G. Native point defects and impurities in hexagonal boron nitride. *Phys Rev B* **97**, (2018).
30. McDougall, N. L., Partridge, J. G., Nicholls, R. J., Russo, S. P. & McCulloch, D. G. Influence of point defects on the near edge structure of hexagonal boron nitride. *Phys Rev B* **96**, (2017).
31. Cofer, C. G. & Economy, J. Oxidative and hydrolytic stability of boron nitride—a new approach to improving the oxidation resistance of carbonaceous structures. *Carbon N Y* **33**, 389–395 (1995).
32. Watanabe, K., Taniguchi, T. & Kanda, H. Direct-bandgap properties and evidence for ultraviolet lasing of hexagonal boron nitride single crystal. *Nat Mater* **3**, 404–409 (2004).
33. Cassabois, G., Valvin, P. & Gil, B. Hexagonal boron nitride is an indirect bandgap semiconductor. *Nat Photonics* **10**, 262–266 (2016).
34. Park, H. *et al.* Large-scale synthesis of uniform hexagonal boron nitride films by plasma-enhanced atomic layer deposition. *Sci Rep* **7**, (2017).
35. Shi, Y. *et al.* Synthesis of few-layer hexagonal boron nitride thin film by chemical vapor deposition. *Nano Lett* **10**, 4134–4139 (2010).
36. Sutter, P., Lahiri, J., Zahl, P., Wang, B. & Sutter, E. Scalable synthesis of uniform few-layer hexagonal boron nitride dielectric films. *Nano Lett* **13**, 276–281 (2013).



37. Sattari-Esfahlan, S. M. *et al.* Low-Temperature Direct Growth of Amorphous Boron Nitride Films for High-Performance Nanoelectronic Device Applications. *ACS Appl Mater Interfaces* **15**, 7274–7281 (2023).
38. Lin, C. M. *et al.* Ultralow-k Amorphous Boron Nitride Based on Hexagonal Ring Stacking Framework for 300 mm Silicon Technology Platform. *Adv Mater Technol* **7**, (2022).
39. Glavin, N. R. *et al.* Amorphous Boron Nitride: A Universal, Ultrathin Dielectric for 2D Nanoelectronics. *Adv Funct Mater* **26**, 2640–2647 (2016).
40. Hong, S. *et al.* Ultralow-dielectric-constant amorphous boron nitride. *Nature* **582**, 511–514 (2020).
41. Zhao, H. *et al.* Atomically Thin Femtojoule Memristive Device. *Advanced Materials* **29**, (2017).
42. Kim, H. G. & Lee, H. B. R. Atomic Layer Deposition on 2D Materials. *Chemistry of Materials* **29**, 3809–3826 (2017).
43. Kim, Y. S. *et al.* Atomic-layer-confined multiple quantum wells enabled by monolithic bandgap engineering of transition metal dichalcogenides. *Sci. Adv* **7**, 7921–7947 (2021).
44. Kumar, P. *et al.* Light–matter coupling in large-area van der Waals superlattices. *Nat Nanotechnol* **17**, 182–189 (2022).
45. Li, H. *et al.* From bulk to monolayer MoS<sub>2</sub>: Evolution of Raman scattering. *Adv Funct Mater* **22**, 1385–1390 (2012).
46. Mak, K. F., Lee, C., Hone, J., Shan, J. & Heinz, T. F. Atomically thin MoS<sub>2</sub>: A new direct-gap semiconductor. *Phys Rev Lett* **105**, (2010).
47. Splendiani, A. *et al.* Emerging photoluminescence in monolayer MoS<sub>2</sub>. *Nano Lett* **10**, 1271–1275 (2010).
48. Sun, Z. *et al.* Statistical Assessment of High-Performance Scaled Double-Gate Transistors from Monolayer WS<sub>2</sub>. *ACS Nano* **16**, 14942–14950 (2022).
49. McClellan, C. J., Yalon, E., Smithe, K. K. H., Suryavanshi, S. V. & Pop, E. High Current Density in Monolayer MoS<sub>2</sub> Doped by AlO<sub>x</sub>. *ACS Nano* **15**, 1587–1596 (2021).

50. Lan, H.-Y., Oleshko, V. P., Davydov, A. V., Appenzeller, J. & Chen, Z. Dielectric Interface Engineering for High-Performance Monolayer MoS<sub>2</sub> Transistors via TaO<sub>x</sub> Interfacial Layer. *IEEE Trans Electron Devices* **70**, 1–8 (2023).
51. Rayner, G. B., O’Toole, N., Shallenberger, J. & Johs, B. Ultrahigh purity conditions for nitride growth with low oxygen content by plasma-enhanced atomic layer deposition. *Journal of Vacuum Science & Technology A: Vacuum, Surfaces, and Films* **38**, (2020).
52. Torsi, R. *et al.* Dilute Rhenium Doping and its Impact on Defects in MoS<sub>2</sub>. *ACS Nano* **17**, 15629–15640 (2023).

## **Acknowledgement**

C.Y.C., R.T., Y.-C. L, and J.A.R. acknowledge funding from NEWLIMITS, a center in nCORE as part of the Semiconductor Research Corporation (SRC) program sponsored by NIST through award number 70NANB17H041. Y.-C.L. acknowledges the support from the Center for Emergent Functional Matter Science (CEFMS) of NYCU and the Yushan Young Scholar Program from the Ministry of Education of Taiwan. C.Y.C. and J.A.R. acknowledge Intel through the Semiconductor Research Corporation (SRC) Task 2746, the Penn State 2D Crystal Consortium (2DCC)-Materials Innovation Platform (2DCC-MIP) under NSF cooperative agreement DMR- 1539916, and NSF CAREER Award 1453924 for financial support. CVD hBN reference for this publication was provided by The Pennsylvania State University Two-Dimensional Crystal Consortium – Materials Innovation Platform (2DCC-MIP) which is supported by NSF cooperative agreement DMR-1539916.

## **Author Contributions**

C.Y.C. conducted the ALD film growth, characterization, and data analysis. Z.S. performed FET device fabrication and electrical measurements. J.A. and Z.C. supervised the FET analysis and discussions. R.T. conducted the CVD growth and film transfer experiments. Y.-C.L. conducted partial characterization, developed quantum well stack, and participated in data analysis. K.W. performed the TEM experiments. B.L. and G.B.R. helped with ALD tool and process development. J.K., Y.-C.L., and J.A.R. supervised the project. All authors participated in the manuscript review.

## **Competing Interests**

The authors declare no competing interests.

## Supplementary Information

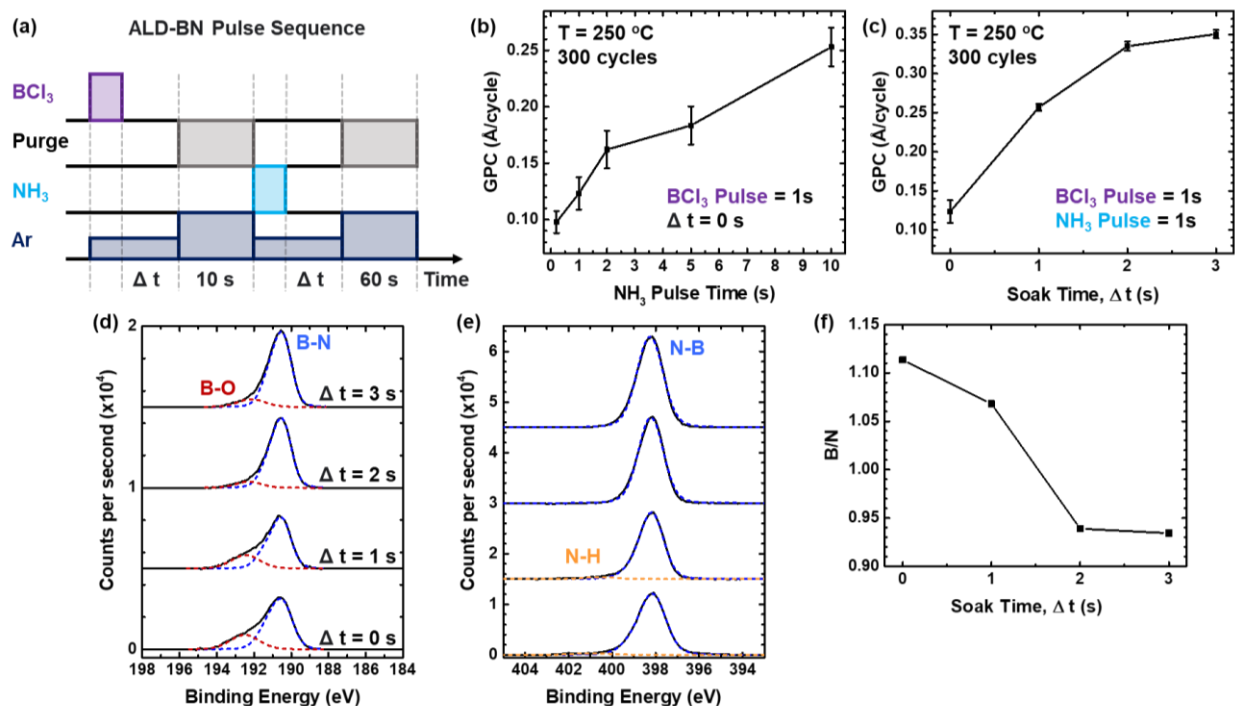
### Tailoring Amorphous Boron Nitride for High-Performance 2D Electronics

Cindy Y. Chen,<sup>1</sup> Zheng Sun,<sup>2</sup> Riccardo Torsi,<sup>1</sup> Ke Wang,<sup>3</sup> Jessica Kachian,<sup>4</sup> Bangzhi Liu,<sup>3</sup> Gilbert B. Rayner, Jr.,<sup>5</sup> Zhihong Chen,<sup>2</sup> Joerg Appenzeller,<sup>2</sup> Yu-Chuan Lin,<sup>6\*</sup> Joshua A. Robinson<sup>1,3,7\*</sup>

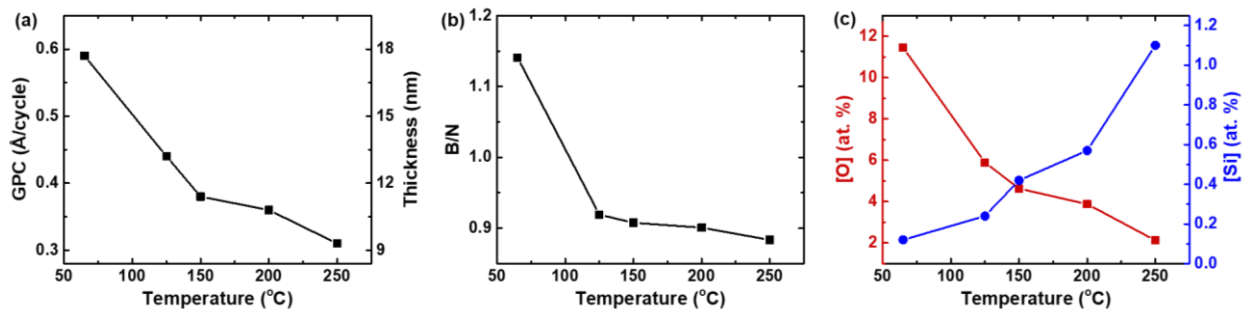
8. Department of Materials Science and Engineering, The Pennsylvania State University, University Park, PA 16802, USA
9. School of Electrical and Computer Engineering and Birck Nanotechnology Center, Purdue University West Lafayette, IN 47907, USA
10. Materials Research Institute, The Pennsylvania State University, University Park, PA 16802, USA
11. Intel Corporation, 2200 Mission College Blvd, Santa Clara, CA 95054, USA
12. The Kurt J. Lesker Company, 1925 PA-51, Jefferson Hills, PA 15025, USA
13. Department of Materials Science and Engineering, National Yang Ming Chiao Tung University, Hsinchu City 300, Taiwan
14. Two-Dimensional Crystal Consortium, The Pennsylvania State University, University Park, PA 16802, USA

\*Yu-Chuan Lin (Email: ycl194@nycu.edu.tw)

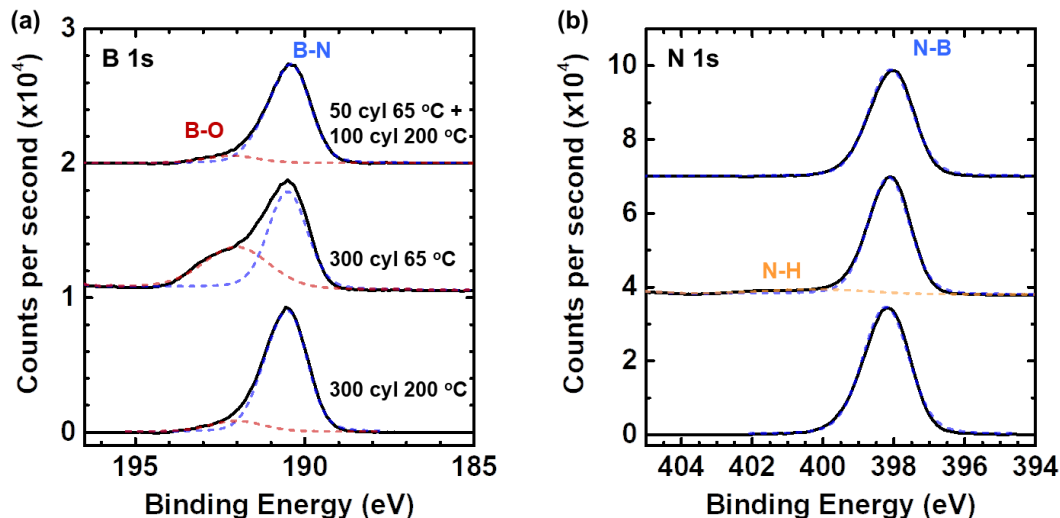
\*Joshua A. Robinson (Email: jar403@psu.edu)



**Supplementary Figure 1:** (a) Schematic of the pulse sequence in ALD of aBN. Precursor and reactant pulses are each followed by a soak step before purging, enabling saturation in aBN growth per cycle (GPC) – likely through increased adsorbate surface coverage after each half cycle - and improving wafer-scale uniformity. GPC is calculated from the average thickness of aBN deposited at 250 °C on a 150 mm Si wafer for 300 ALD cycles. Purge times after the  $\text{BCl}_3$  and  $\text{NH}_3$  pulse and soak steps are 10 and 60 s, respectively. (b) GPC as a function of  $\text{NH}_3$  pulse time with no soak times. (c) GPC as a function of soak time at pulse times of 1 s for both  $\text{BCl}_3$  and  $\text{NH}_3$ . As soak time increases, the variation in thickness across the 150 mm Si wafer decreases significantly, indicating improved wafer-scale uniformity. (d) B 1s and (e) N 1s core level XP spectra corresponding to the aBN films shown in (c). (f) Film stoichiometry B/N quantified from B 1s and N 1s spectral regions corresponding to the aBN films shown in (c).



**Supplementary Figure 2:** The deposition temperature dependence of aBN film properties is investigated for aBN deposited on Si wafers from 65 – 250 °C for 300 ALD cycles. (a) GPC and average thickness of aBN deposited from 65 – 250 °C. (b) B/N ratio quantified from B 1s and N 1s spectral regions in XPS of aBN films deposited from 65 – 250 °C. (c) O and Si concentrations quantified from the B-O binding energy component of the B 1s peak and the Si 2p spectral region, respectively, in XPS of aBN deposited from 65 – 250 °C. It is assumed that all oxygen within the aBN film is bound to boron.



**Supplementary Figure 3:** (a) B 1s and (b) N 1s core level XP spectra of aBN deposited at different temperatures on Si substrates. The pure 65 and 200 °C aBN films have a thickness of 17.6 and 11.2 nm, respectively. When 65 °C aBN is immediately followed by aBN deposition at 200 °C without sample removal into ambient environment, the oxidation level measured for the hybrid aBN film stack is significantly lower than that estimated for the hybrid aBN film stack using oxidation levels of the pure 65 °C- (i.e., aBN resulting from deposition at 65 °C only) and pure 200 °C- (i.e., aBN resulting from deposition at 200 °C only) aBN films and accounting for the 65 °C- and 200 °C-aBN ALD thickness contributions to the hybrid aBN film stack (see text below).

Comparison of (1) the measured O at% in the hybrid aBN film stack and (2) the estimated O at% in the hybrid aBN film stack is shown below. The estimation assumes the 65 °C-aBN component film of the hybrid aBN film stack is not transformed by the subsequent in situ 200 °C aBN ALD and is oxidized ex situ (poor capping by the 200 °C-aBN component film of the hybrid aBN film stack) and/or in situ.

(1) Measured O at% in hybrid aBN film stack = 3.0%

(2) For the hybrid aBN film stack (aBN ALD at 65 °C followed by aBN ALD at 200 °C, all in situ), thickness for each component aBN layer and thickness of the hybrid aBN film stack can be calculated based on the number of ALD cycles completed for each component deposition and the GPC for aBN ALD at 65 and 200 °C from **Supplementary Figure 2a:**

50 cycles \* 0.59 Å/cycle = 29.5 Å (2.95 nm) of 65 °C aBN

100 cycles \* 0.36 Å/cycle = 36 Å (3.6 nm) of 200 °C aBN

Total hybrid aBN film stack thickness = 2.95 nm + 3.6 nm = 6.55 nm (45% 65 °C aBN, 55% 200 °C aBN)

From **Supplementary Figure 2c**, the O concentrations in the pure 65 °C- (i.e., aBN resulting from deposition at 65 °C only) and pure 200 °C- (i.e., aBN resulting from deposition at 200 °C only) aBN films are 11.4% and 3.9%, respectively. Using these O concentration values, the estimated O at% in each component film of the hybrid aBN film stack and the estimated O at% in the entire hybrid aBN film stack are as follows:

$0.45 * 11.4\% = 5.1\%$  (estimated O at% in 65 °C aBN component of the hybrid aBN film stack)

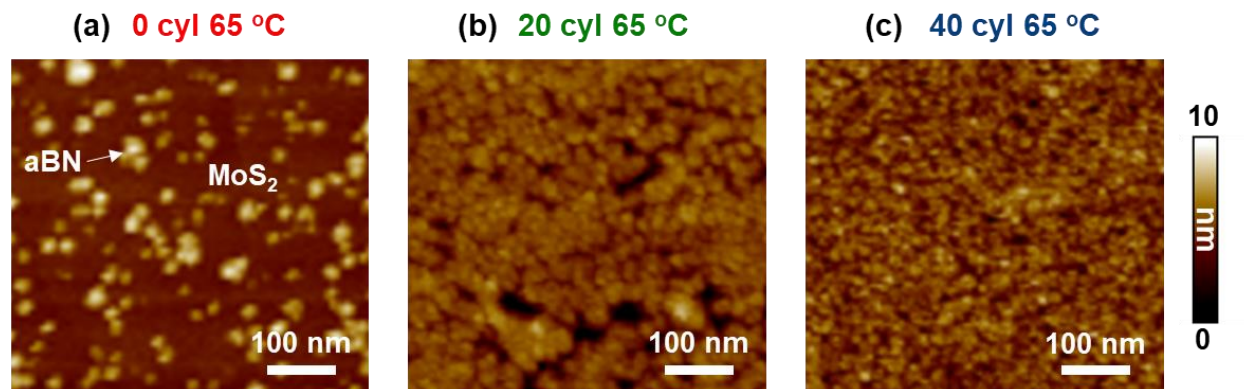
$0.55 * 3.9\% = 2.2\%$  (estimated O at% in 200 °C aBN component of the hybrid aBN film stack)

The estimated O at% in the entire hybrid aBN film stack = 7.3%.

The estimated (versus measured) O at% in the entire hybrid aBN film stack is > 2× higher.

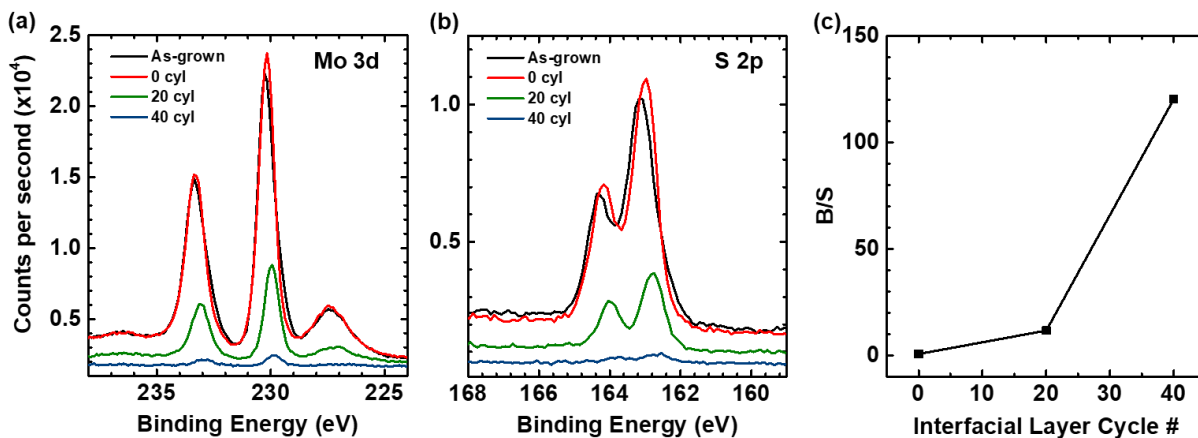


X cycle 65 °C interfacial layer + 300 cycle 250 °C aBN

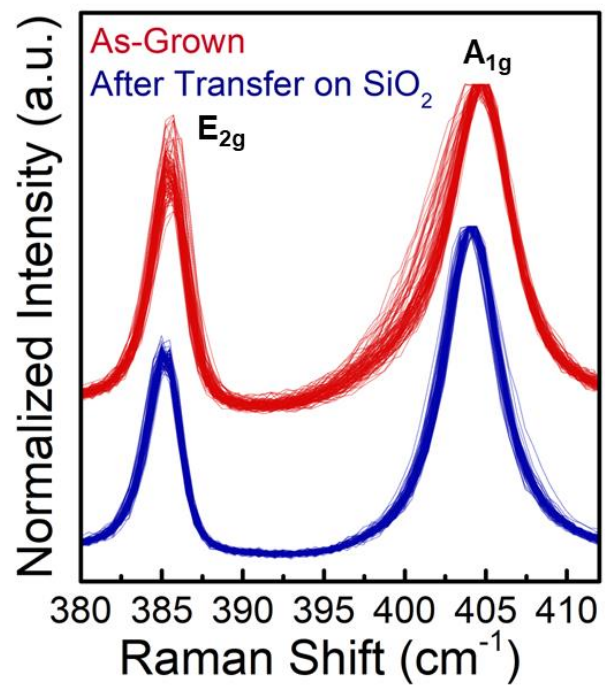


**Supplementary Figure 4:** AFM image of aBN deposited on MoS<sub>2</sub> with (a) 0, (b) 20, and (c) 40 cycles of the 65 °C aBN interfacial layer, which is immediately followed by 300 cycles of 250 °C aBN deposition. Coalescence of the aBN film occurs when at least 40 cycles of the 65 °C interfacial layer is integrated.

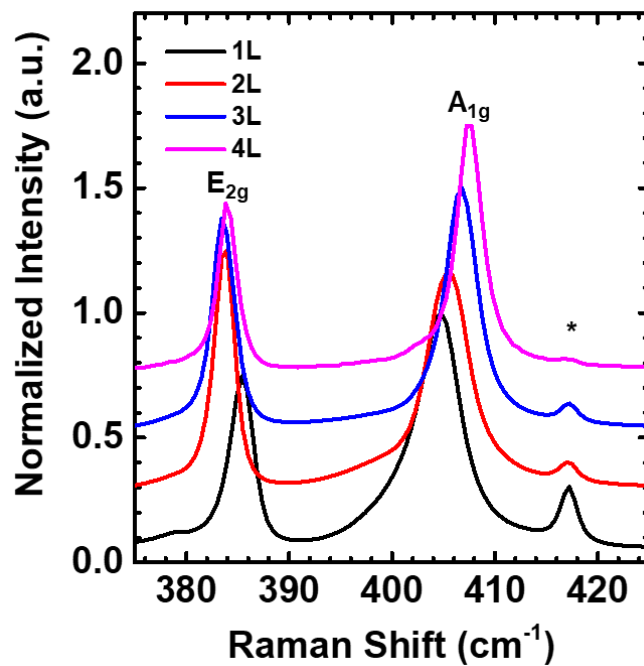
X cycle 65 °C interfacial layer + 300 cycle 250 °C aBN



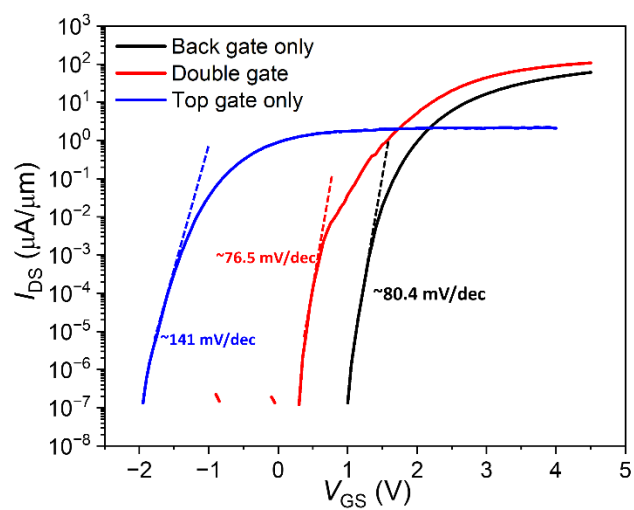
**Supplementary Figure 5:** (a) Mo 3d and (b) S 2p XP spectra of as-grown and aBN-capped MoS<sub>2</sub>. All aBN encapsulation begins with varying number of ALD cycles of the 65 °C interfacial layer, followed by 300 cycles of 250 °C aBN. (c) B/S ratio calculated from quantification of B 1s and S 2p XP spectral regions shows exponential increase in B signal with increasing interfacial layer ALD cycles, indicating enhanced nucleation of aBN at 40 cycles of the interfacial layer. B/S~0 for 0 cycles of interfacial layer highlights that significant aBN nucleation at 250 °C on MoS<sub>2</sub> cannot occur without the integration of an interfacial layer.



**Supplementary Figure 6:** Raman spectra of as-grown and transferred monolayer MoS<sub>2</sub>. The E<sub>2g</sub> and A<sub>1g</sub> peak FWHM decreases after transfer, indicating a release of the strain induced by the growth substrate.



**Supplementary Figure 7:** Raman spectra of as-grown 1-4L MoS<sub>2</sub> on c-plane sapphire. The peak separation between E<sub>2g</sub> and A<sub>1g</sub> increases as layer number increases. \* denotes the sapphire substrate Raman peak.



**Supplementary Figure 8:** Transfer curves of a double gated ML MoS<sub>2</sub> FET under different gate operation modes, including back gate only sweep (top gate floating), double gate sweep with top and bottom gate connected, and top gate only sweep (back gate floating).